ORIGINAL ARTICLE

Excavation-induced deformation and stress responses of a highway tunnel in fault fracture rock zone with high geo-stress: a case study of Xiangjunshan tunnel

Rongming Zhou[1] · Xiaolin Weng[1] · Lin Li[1] · Yanwei Guo[2] · Siyu Chen[3] · Xiaoming Huang[3]

Abstract

Tunnel excavation in high geo-stress shattered fault zone usually causes lining cracking, tunnel collapse and arch settlement because of rock fragmentation, low strength and poor stability of surrounding rock. This paper takes Xiangjunshan tunnel in high in-situ stress fault fracture zone in Sanmenxia, China, as an example. The field monitoring tests included surrounding rock deformation monitoring, surrounding rock-initial support, shotcrete, steel arch and primary support-secondary lining stress measurement. These tests were utilized to study the deformation law and stress response of six sections in Class IV and V rock mass during the tunnel construction. Test results showed that the tunnel deformation of fault fracture zone was asymmetrical during excavation. The surrounding rock stress presented a discrete distribution in space, the stress variation trend of shotcrete and steel frame was not coordinated. The stress of shotcrete reached 75% of its peak value in the initial stage, while the stress of steel frame reached its peak value in about 1 month. The temporal distribution curve of primary support-secondary lining stress indicated three stages of intense growth, quick development and steady development stage in the construction. The research results give significant insights and guidelines for tunnel construction in similar geological conditions.

Keywords Tunnel engineering · High in-situ stress · Fault fracture zone · In-situ monitoring · Stress responses

✉ Xiaolin Weng
2019021012@chd.edu.cn

Rongming Zhou
2018121096@chd.edu.cn

Lin Li
lilin_sanmao@163.com

Yanwei Guo
2019021011@chd.edu.cn

Siyu Chen
chsy@seu.edu.cn

Xiaoming Huang
Huangxm@seu.edu.cn

[1] Key Laboratory for Special Area Highway Engineering of Ministry of Education, Chang'an University, Xi'an 710064, China

[2] Henan Communications Planning and Design Institute Co., L T D., Zhengzhou 450018, China

[3] School of Transportation, Southeast University, Nanjing 21189, China

Introduction

Since the scale of road and railway construction in Midwest China is increasing yearly, tunnels have played an increasingly important role in transport engineering. At the same time, an increasing number of mountain tunnels have emerged to meet the growing demand for transport capacity, such as Huangjiazhai tunnel (Bian et al. 2019), Satomi tunnel (Gao et al. 2014), Xinzhuangling tunnel (Lai et al. 2017), Baicheng tunnel (Qiu et al. 2022), Yanmenguan tunnel (Lin et al. 2017). These tunnels inevitably encounter challenging conditions, such as high ground stress (Zhang et al. 2020, Manasa and Maji 2023), fracture zones (Zhong et al. 2020; Das et al. 2018), landslides (Zhang et al. 2022; Gattinoni et al. 2019), falling stones (Qin et al. 2022), karst strata (Gisbert et al. 2009), large deformations in the surrounding rock and rich groundwater zones (Xu et al. 2022; Wu et al. 2022) during construction. Especially tunnels are excavated in the fault zone of high geo-stress areas, engineering problems such as tunnel palm face collapse and large deformation often occurred due to fragile rock mass and weak stability

of surrounding rock (Wang et al. 2015; Meng et al. 2013; Bayat and Hamidi 2017; Roy et al. 2017; Yang et al. 2017). Thus, it is of significant engineering meaning to research the distribution of rock mass deformation and stress responses of supporting structures of tunnels crossing fault fracture zone of high in-situ stress areas.

Fault zones frequently encounter poor geological conditions in the construction of mountain tunnels (Zhong et al. 2020). It causes significant changes in the rock structure and leads to asymmetric ground stress, meanwhile, this is the primary factor contributing to asymmetric stress distribution in deeply buried tunnels (Jeon et al. 2004; Wang et al. 2017a, b; Li et al. 2011). In the high geo-stress zone, rock mass deformation and load-bearing capacity are the most critical affecting factors affecting mountain tunnels' stability (Chen et al. 2019a; Deng et al. 2022; Wang et al. 2016; Qian et al. 2017). To solve the complex construction problem of tunnel crossing through fault, many researchers at home and overseas have launched a series of research. For different tunnel excavation methods and geological engineering conditions, scholars have used different research methods, such as field tests, to develop reasonable support design solutions (Chen et al. 2022; Su and Fu 2009; Liu et al. 2010, Dwivedi et al. 2013, Maleki et al. 2018). Asghar et al. (2017) used numerical model to study the mechanical behavior of rock mass, and calculated the displacement value of tunnel vault. Malkowski et al. (2017) analyzed the influence of fault fracture zone on the convergence deformation of mine tunnel and the degree of fracturing around the tunnel by numerical method, and verified the accuracy of the calculated results by comparing with the field measured tunnel convergence data. The surrounding rock and tunnel lining stress distribution characteristics are also important contents of current research (Zhou et al. 2021a). Combining numerical simulations and field tests, scholars have compiled a wealth of engineering examples to understand the characteristics of tunnel envelope pressure evolution under high-ground stress and to address the impact of excessive tunnel deformation on tunnel construction progress and safety (Wang et al. 2019; Aicha and Mezhoud 2021; Tang and Ren 2021). However, the types of fault zones and high-ground stress conditions encountered in mountain tunnels differ. The rock mass's mechanical properties, interaction effects, and support structure are also different (Wu et al. 2022). There are relatively few studies on spatiotemporal effect of rock deformation and stress characteristics of the tunnel support structure with complex conditions in high geo-stress fault fracture zones and force characteristics of the support structures, and further studies are needed to optimize the support methods to enhance tunnel safety and rock bearing capacity (Chen et al. 2019b; Zhou et al. 2021b; Li et al. 2022; Lia et al. 2018). Besides, there needs to be effective experience and construction guidance for tunnel construction and support design.

In this paper, taking the Xiangjunshan tunnel of Luan Lu Highway project in Henan Province as the engineering background, excavation-induced deformation and stress responses for the tunnel in high geo-stress fault fracture zones were analyzed in detail. Firstly, tunnel deformation monitoring tests were used to analyze the arch settlement and perimeter convergence of Grade IV and V rock sections; then, according to the results of stress measurements, spatial and temporal distribution of the surrounding rock stress and support system stress with time were determined; finally, tunnel support methods were optimized following the maximum tunnel deformation and stress evolution characteristics of the tunnel over time. The findings can provide optimal support systems and construction guidance for the Xiangjunshan tunnel and provide the theoretical basis for the constructing similar tunnels crossing high in-situ stress fault fracture zone.

Project overview

Luan Chuan-Lu Shi expressway project is one of ten lines in Henan province's expressway network scheme (Fig. 1). The total length of expressway project is 75 km at 80 km/h, running between Luoyang and Sanmenxia. It is located in the mountainous region of western Henan, passing east of the Qinling Mountains, south of the Funiu Mountains and west of the Xionger Mountains. The Xiangxianshan tunnel is located in a complex tectonic zone in the Qinling Mountains, where the latitudinal tectonic system is particularly developed. Therefore, highway construction in this area is more challenging. It is a separate tunnel with a distance of 9–47 m between two lines. The left line starts and ends at Z4K52+612 to Z4K58+120, its length and maximum buried depth are 5508 m and 396 m, respectively; the right section starts and ends at K52+627 to K58+124, its length is 5497 m; and its maximum buried depth is 395 m. Both left and right lane tunnels have a clear width of 10.25 m and a clear height of 5 m.

Geological structures

According to the regional tectonic data and physical survey data of Henan Province, the tunnel is particularly well developed in the latitudinal tectonic system, with the main fault being the Taowan Fault. There are two faults, F1 and F2, at the tunnel body (F1 and F2 faults in Fig. 2). F1 intersects with the tunnel left line at Z4K53+869, and the tunnel right line at K53+853, with an angle of about 56°. F2 intersects with the left line of the tunnel at Z4K55+830 and the right line at K55+844, with an angle of about 78°. The grade of surrounding rock for fault fracture zones and their affected areas are mainly V and IV. Tunnels in the fault
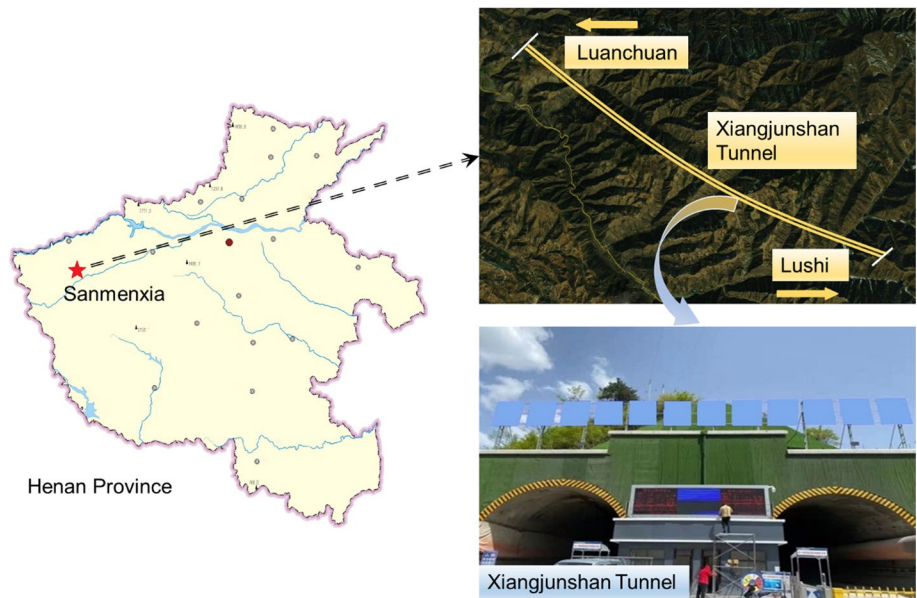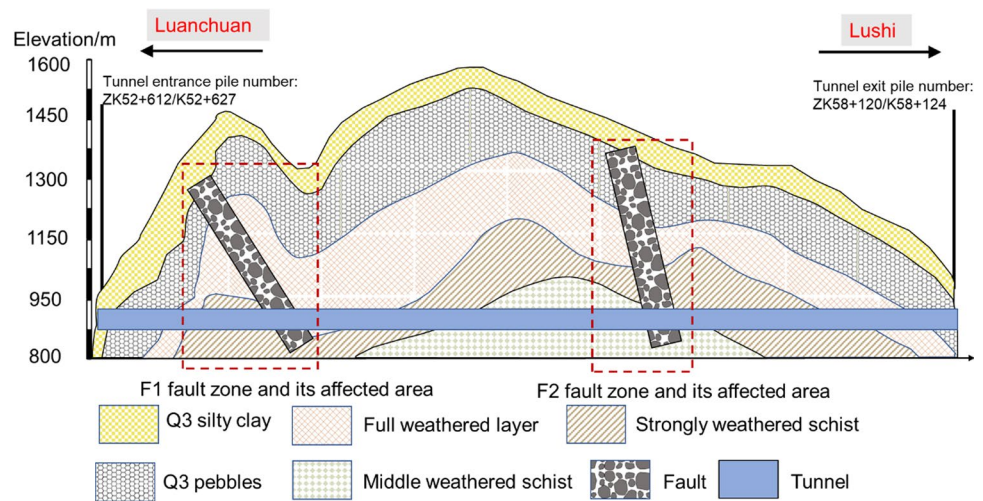
Fig. 1 Location of Xiangjun-shan tunnel

Fig. 2 Geological section along the Xiangjunshan Tunnel

zone are prone to collapses, rock falls and other engineering accidents.

Rock mass properties and hydrogeology

According to the engineering geological survey, the tunnels' overlying strata mainly formed from the Quaternary Upper Pleistocene (Q3) silty clay, pebbles and the Proterozoic Taowan Formation schist below the underlying bedrock. The geological section along the tunnel is presented in Fig. 2. The detailed information and distribution of the strata are as follows: Q3 silty clay contains quartz minerals and a small amount of root and leaves, and the soil layer is about 0–2 m thick, mostly distributed at the foot of the slope. Q3 pebbles are mainly schist, with a thickness of about 2–3 m, and they are mostly distributed near the foot

of the slope. The Lower Palaeozoic Taowan Formation schist includes fully weathered, strongly weathered and moderately weathered layers. The full weathered layer is about 3 m thick, and the original rock structure has been largely destroyed, with extremely developed joints and fissures. The strong weathered layer is about 14–36 m thick and the joints and fissure are developed. The weathered middle layer is thicker, with more developed joints and fissures and a small amount of rock in fragmented form. The main types of underground water in the tunnel area are bedrock crack water and loosely packed rock pore water. The loose rock pore water is shallowly buried and mainly localized in the Pleistocene gravel soil layer. The tunnel area is dominated by bedrock fissure water, and groundwater flows into the tunnel along the rock fractures, resulting in dripping water. Particularly during the rainy season,

there may be sudden water surges in the locally fractured rock, causing tunnel collapse.

Geo-stress

The geo-stress results measured using hydraulic fracturing are presented in Fig. 3 and Table 1. Table 1 shows that the geo-stress field is characterized by principal horizontal stress, the maximum of which is in the direction of N 25° E. There is a critical depth above which the minimum horizontal stress is greater than the vertical stress, and the situation is the opposite below the depth. The average values of maximum and minimum lateral stress coefficients are 1.31 and 0.94, respectively. According to the standard for engineering classification of rock mass (GB/T 50218-94, National standards of the People's Republic of China, 1995), when the ratio of uniaxial saturated compressive strength of the rock (R_c) to the maximum initial ground stress in the direction of the vertical cave axis (σ_{max}) is between 4 and 7, the rock mass is in the high geo-stress state. The tunnel ground investigation data shows that $R_c = 44.4$ MPa, $\sigma_{max} = 8.14$ MPa, so $R_c/\sigma_{max} = 5.45$. Therefore, the test section is in the high geo-stress zone. When high geo-stress sections are encountered during tunnel construction, rock bursts easily occur. Because of the

fault fracture zones, the tunnel is easily susceptible to collapse during excavation.

Construction method and support design

The width and height of a typical tunnel section were 12.7 m and 10.3 m, respectively. The tunnel excavation was carried out with a full section drill and blast method near the fault rupture zone and step method in the fractured fault zone, as illustrated in Fig. 4.

When excavating the reserved core soil, the upper step excavation height was 4.5 m, the width was 6 m, the length was 0.8 m, the core soil was 2 m from the vault, and the length was 3 m. The staggered excavation length was 1.5 m for the left and right sections. The invert was excavated and supported in half swing, and a trestle bridge was laid on its upper side. Shotcrete was sprayed immediately after the invert was excavated to make the primary support structure into a ring as quickly as possible. The support system of the tunnel included advance support and initial support. The main support consisted of steel flower pipes, shotcrete, anchors and steel arches. The shotcrete thickness was 30 cm, and the reserved space between the initial support and the rock mass was 15 cm.
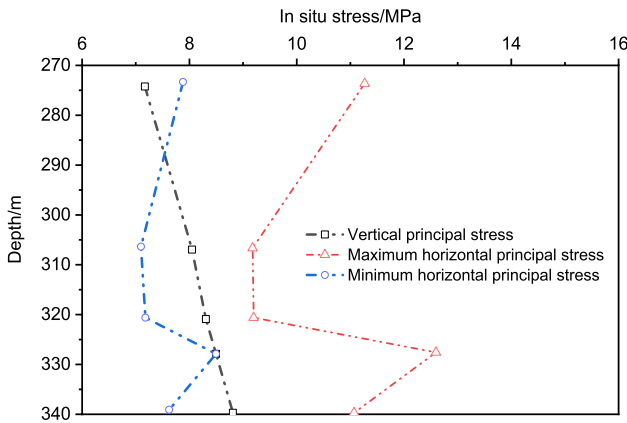
In-situ monitoring procedure

For the sake of studying excavation-induced deformation and stress responses of the tunnel, a range of field monitoring tests were planned in Xiangjunshan tunnel:
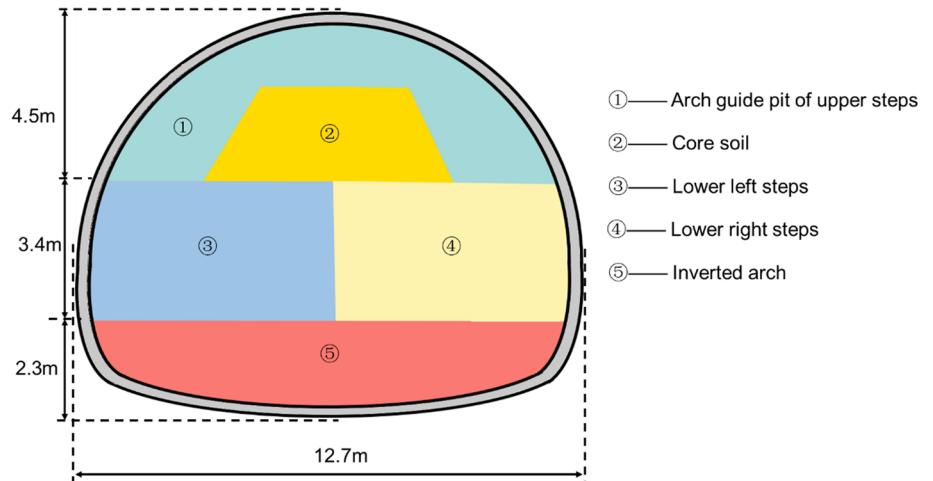
- vault settlement and peripheral convergence monitoring
- surrounding rock-initial support stress monitoring
- shotcrete stress measurement
- steel frame stress measurement
- primary support-secondary lining stress monitoring.

The field deformation monitoring test of Xiangjunshan tunnel included items vault settlement and perimeter

Fig. 3 In situ stress distribution curve with depth

Table 1 Geo-stress results of the test section

Depth (m)	Value of geo-stress (MPa)			Direction of S_H	$\frac{S_H}{S_V}$	S_h/S_V
	Maximum horizontal principle stress S_H	Minimum horizontal principle stress S_h	Vertical principle stress S_V			
273.20–338.98	9.09–12.53	7.04–8.41	7.08–8.76	N 25° E	–	–
273.20–273.82	11.17	7.87	7.08	–	1.58	1.11
306.03–306.65	9.09	7.04	7.93	–	1.15	0.89
320.05–320.67	9.12	7.09	8.29	–	1.10	0.86
327.28–327.98	12.53	8.41	8.48	–	1.48	0.99
338.36–338.98	10.99	7.57	8.76	–	1.25	0.86

Fig. 4 Excavation method of the step method

- ① —— Arch guide pit of upper steps
- ② —— Core soil
- ③ —— Lower left steps
- ④ —— Lower right steps
- ⑤ —— Inverted arch

convergence, measured by Leica total station and explicit digital convergence and reflective patch, respectively. The observation time of tunnel deformation is 90 days. A vibrating string earth pressure gauge measured the surrounding rock stress. The accuracy of the earth pressure gauge is selected as 0.2 MPa, 0. 6 MPa, and 2 MPa respectively. The layout point of the earth pressure box should have a certain flatness to make the earth pressure gauge contact the surrounding rock well. In order to ensure the reliability of the measurement results of the earth pressure gauge, the earth pressure gauge is connected with the 8-channel vibrating string acquisition instrument and the data cloud platform, and the debugging is carried out.

An embedded concrete strain gauge measured shotcrete stress, and steel arch stress was measured by a surface strain gauge, of which two surface strain gauges were set up at each measuring point. The test components are shown in Fig. 5. The measurement accuracy of embedded concrete strain gauge and surface strain gauge for steel arch is 0.01 MPa respectively. The initial frequency of the strain gauge is detected before installing the strain gauge, and then the surface strain gauge support is fixed at the monitoring position of the steel frame and fixed with bolts, and a metal protective shell is installed to place the strain gauge to be damaged. The embedded strain gauge is fixed at the steel frame and steel mesh with cable ties. After the

Fig. 5 Site layout of test instruments. **a** Reflective patch; **b** earth pressure gauge; **c** surface strain gauge; **d** concrete strain gauge
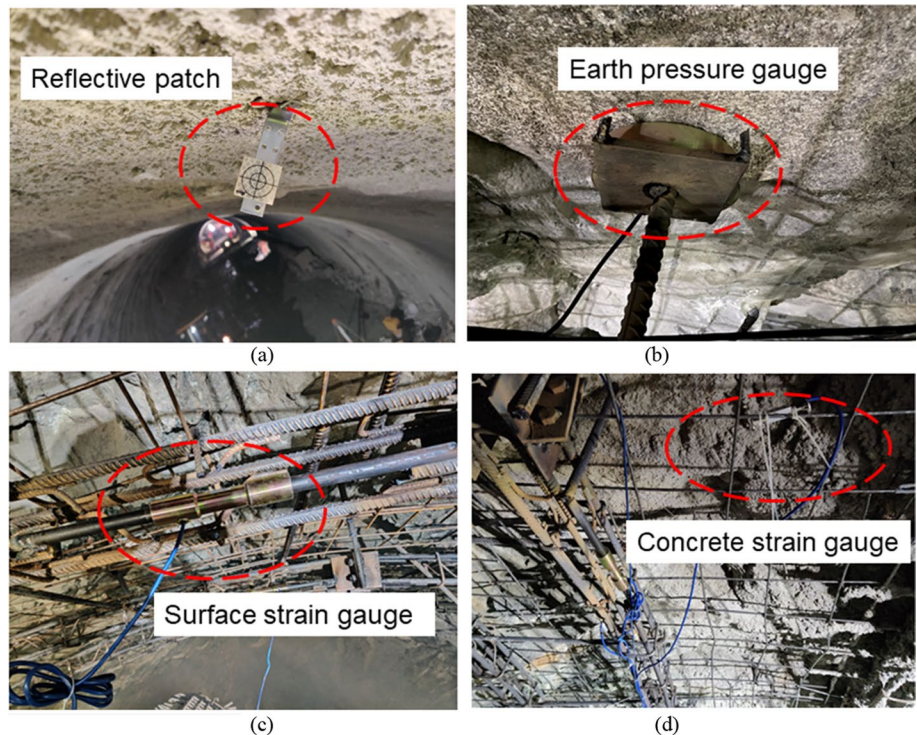
strain gauge is installed, it is debugged to ensure the validity and accuracy of the measurement data.

The hand-held vibrating string acquisition instrument collected all measured data, and the collection frequency was 1 time/day. The acquisition instrument could stop data collection when the collected data no longer changed significantly. The monitoring time of the primary lining-surrounding rock pressure and the pressure between the primary and secondary lining is also 90 days. The monitoring time of shotcrete stress and steel arch stress is 120 days. Near the fault fracture zone of Grade IV rock mass, ZK53 + 830 and ZK53 + 950 were selected as test sections, and in the fractured fault zone of Grade V rock mass, ZK53 + 860, ZK53 + 880, ZK53 + 900 and ZK53 + 920 were selected as test sections.

Analysis of tunnel deformation monitoring

Monitoring points of vault settlement and peripheral convergence are shown in Fig. 6. Three test points, G1, G2 and G3, were set to measure the vault settlement. The test section selected two lateral lines, BC and GC, to measure the peripheral convergence. Two monitoring sections were selected, numbered ZK53 + 830 and ZK53 + 860. Cumulative settlement curves of the tunnel vault and perimeter over time are shown in Fig. 7.

As for the ZK53 + 860 section in Fig. 7a, tunnel deformation consisted of three stages: intense development stage, rapid development stage and steady development stage. During the construction, there was a significant spatial and temporal effect of vault settlement and peripheral convergence, with cumulative settlement stabilizing after 30 days. In the intense growth stage, the maximum cumulative settlement of G1, G2 and G3 were 58.7 mm,
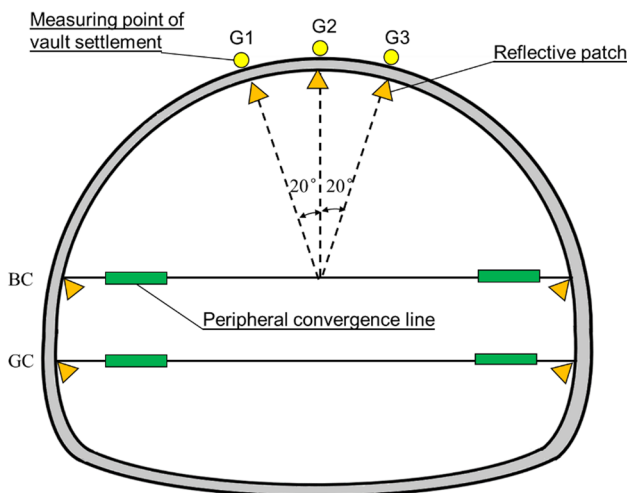

Fig. 7 Vault settlement and peripheral convergence of each monitoring section. **a** ZK53 + 860; **b** ZK53 + 830

Fig. 6 Measurement lines and points layout of Xiangjunshan Tunnel

40.3 mm and 52.1 mm, accounting for 80%, 76% and 75% of the total settlement, respectively. There are two reasons for this. On the one hand, there was insufficient space reserved between the arch crown and the rock mass during site construction; For another, the redistribution of the rock mass pressure after excavation and the coordination of deformation between the rock mass and the initial support resulted in rapid tunnel deformation rate. The convergence rate of survey line BC and GC was significantly higher than the vault settlement rate, indicating that the surrounding rock horizontal deformation of the high-ground stress tunnel was significantly higher than the vertical deformation. In the rapid deformation stage (8–27 days), the average settlement rate of G1, G2 and G3 measurement points was 0.41, 0.29 and 0.47 mm/day, respectively, indicating that the vault settlement rate was significantly lower than that of the arch shoulder settlement in this period. The horizontal convergence rate of BC and GC survey line was 0.41 and 0.93 mm/day, respectively,

indicating that the GC survey line was greatly affected by invert and lower step excavation in this period.

As for the ZK53+830 section in Fig. 7b, tunnel deformation also included three development stages: intense development stage, rapid development stage and slow development stage. In the intense deformation stage (0–18 days), the deformation rate was significantly slower than that of the ZK53+860 section. The mean values of arch subsidence and perimeter convergence were 15.9 mm and 18.1 mm, amounting to 55% and 51% of the accumulated total subsidence, respectively. After the secondary lining construction, the vault settlement and the peripheral convergence ratio slowed down, which showed that secondary lining had an obvious impact on controlling the settlement in tunnel crossing the high geo-stress fractured fault zone. The convergence rate of BC survey line kept up after the secondary lining construction, suggesting that the horizontal deformation of rock mass near the fault fracture zone was larger than vertical deformation, so supporting structure stiffness of tunnel arch can be appropriately increased in the subsequent construction process.

Tunnel primary support stress test results

Data processing of stress

The change of surrounding rock pressure causes the deformation of the bearing film of the earth pressure box, and the deformation changes the tension of the steel string and affects the vibration frequency of the steel string. The surrounding rock pressure can be calculated according to the following formula (1).

$$P = K \times \left(f_i^2 - f_0^2\right), \tag{1}$$

where P is the measured earth pressure (unit: MPa), K is the instrument calibration coefficient (unit: MPa/Hz^2), f_i is the measured frequency (unit: Hz), f_0 is the initial frequency (unit: Hz).

The concrete strain gauge and surface strain gauge for steel arch vibrating wire strain gauges, which are composed of a strain gauge tube, a coil protection housing, a steel string and a coil, and the steel string and the coil are used to measure the vibration frequency. The strain value can be calculated by Eq. (2):

$$\varepsilon = k \times \left(f_i^2 - f_0^2\right), \tag{2}$$

where ε is the strain value, k is the linear relationship function between the output frequency value and the compressive stress value (unit: 1/Hz^2).

Further, the stress of steel arch and shotcrete can be obtained according to formula (3):

$$\sigma = E \times \varepsilon, \tag{3}$$

where σ is the stress value (unit: MPa), E is the elastic modulus of the material, and ε is the strain value calculated by formula (2).

Development and distribution of surrounding rock stress

Two sections were selected from the total monitoring sections to monitor surrounding rock stress, numbered ZK53+830 and ZK53+880. There were nine measuring points in respect of each monitored section in Fig. 8. The positive value presents the compression. As for the ZK53+830 section, the stress increased dramatically before the primary support closure. After that, the surrounding rock pressure at measurement points 7 and 8 changed to a lesser extent, while the surrounding rock pressure at other measurement points appeared to decrease and then increase. After the second lining construction, the surrounding rock pressure stabilized. Compared with the arch crown stress, the horizontal stress on the arch shoulder and haunch was greater, indicating that the horizontal tectonic stress was obvious. Figure 10a showed that the maximum stress at left haunch and arch shoulder was 0.212 MPa and 0.234 MPa, respectively, while the maximum pressures at the right haunch and spandrel were 0.179 MPa and 0.159 MPa, respectively. The surrounding rock stress was distributed asymmetrically about the tunnel axis and discrete in space. The construction of the second lining can effectively reduce the pressure at the spandrel and waist.

As seen in Fig. 9b, before the construction of lower steps, the surrounding rock pressure at measurement points H0–H4 increased rapidly due to the large stress change induced by the upper step excavation. After the
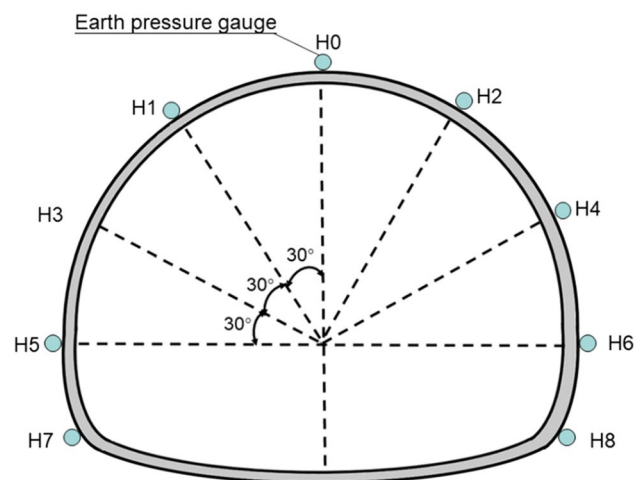

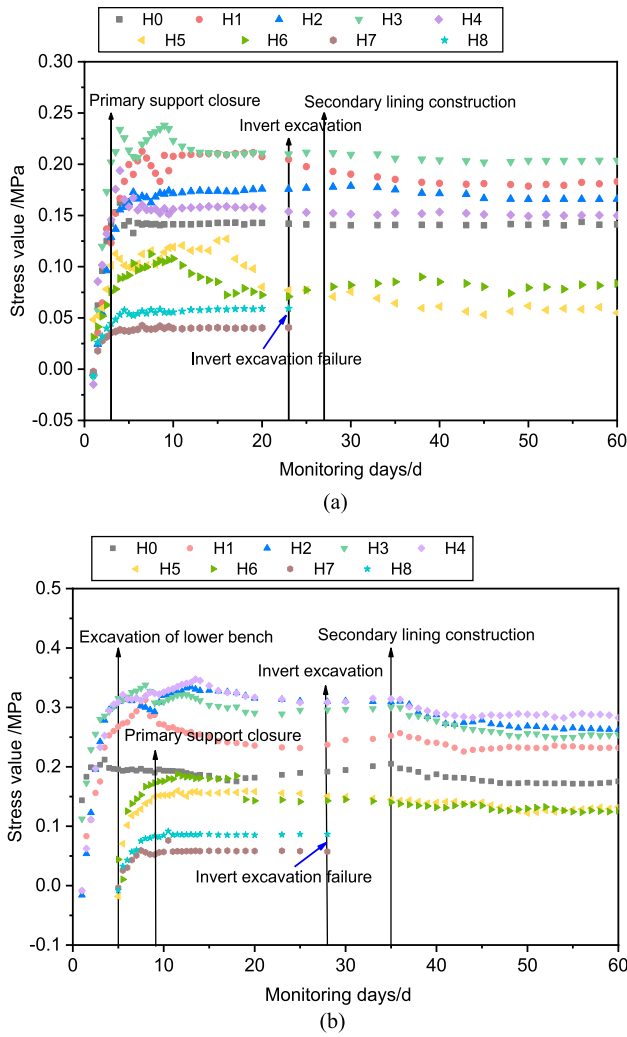**Fig. 8** Distribution of stress measurement points

(a)

(b)

Fig. 9 The distribution curve of the surrounding rock stress over the time of each section. **a** ZK53 + 830; **b** ZK53 + 880
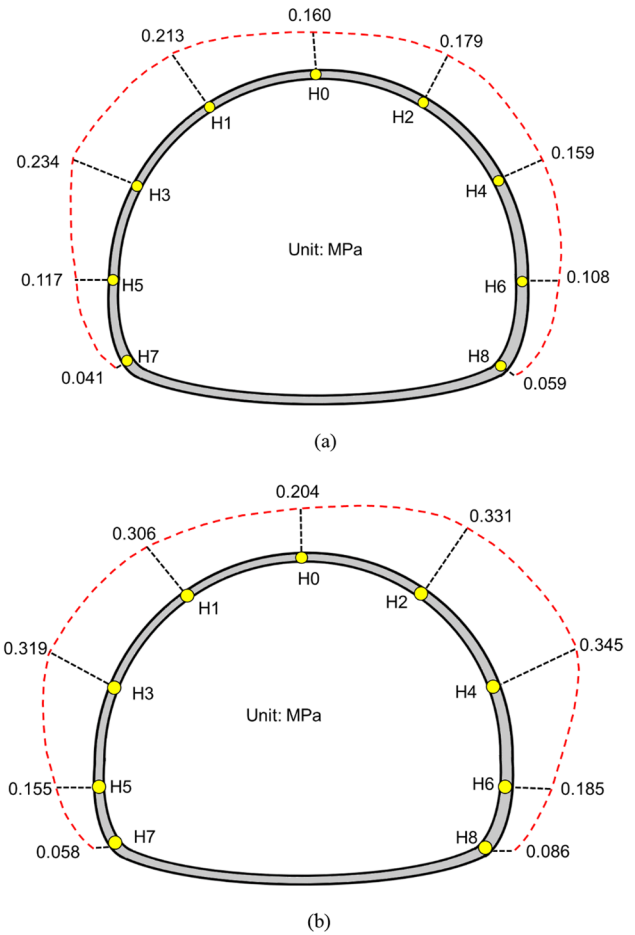

(a)

(b)

Fig. 10 Envelope of maximum internal forces between the surrounding rock and initial support (unit: MPa). **a** ZK53 + 830; **b** ZK53 + 880

Development and distribution of shotcrete stress

Two sections were selected from the total monitoring sections to monitor shotcrete stress, numbered ZK53 + 830 and ZK53 + 900. There were seven measuring points in each monitoring section, as shown Fig. 11. Stress distribution curve of shotcrete with time is seen in Fig. 12. And the variation curve of maximum shotcrete stress is shown in Fig. 13.

C25 concrete was used as the shotcrete, and its compressive and tensile strength were 16.7 MPa and 1.78 MPa, respectively. As seen in Fig. 12, shotcrete stress (except arch feet) had rapidly grown before the secondary lining construction. After the secondary lining construction, the stress at C1–C2 increased and then gradually decreased, followed by a slight increase and eventual stabilization. However, the stress of C0 increased first and then decreased, and gradually became regionally stable. There are two reasons to explain this phenomenon: one is that the concrete in the trolley appears to have a hydration heat reaction in the hardening process; on the other hand, during the construction

initial support was completed, the surrounding rock pressure at measurement points H2–H4 first increased slowly, then decreased gradually, while measurement point H1 gradually decreased, indicating that the initial support could effectively govern the stress release in the rock. After the completion of the secondary lining construction, the contact stress first slowly decreases and then tends to be stable, which indicates that the secondary lining of the section where the fault fracture zone is located has a better supporting effect. In Fig. 10b, the maximum compressive stress of section ZK53 + 880 appeared at H4, and it was 0.345 MPa. The rock mass stress was spread symmetrically along the tunnel axis, with a value of 0.058–0.345 MPa.
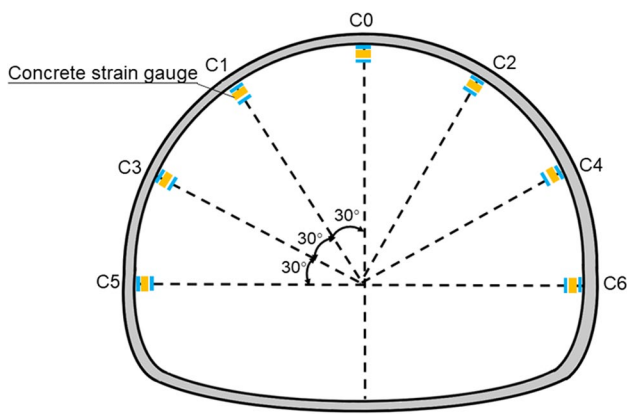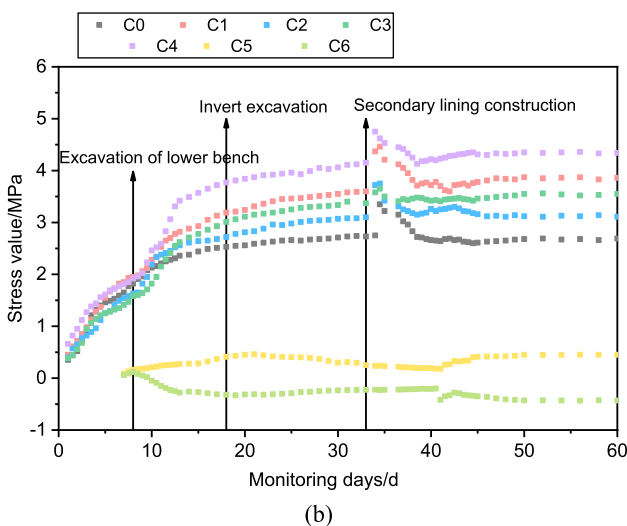
Fig. 11 The monitoring points of shotcrete stress
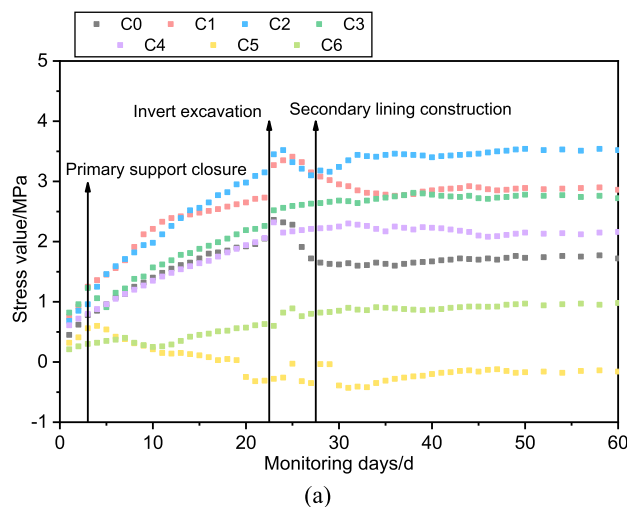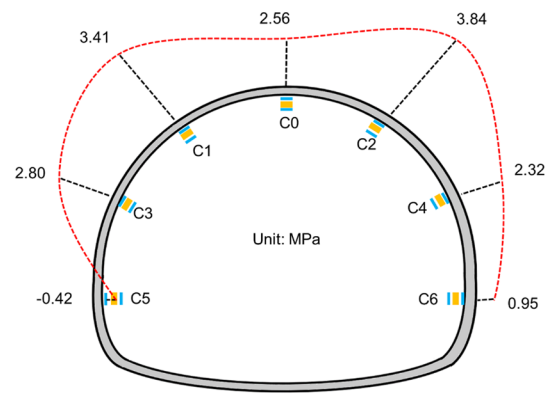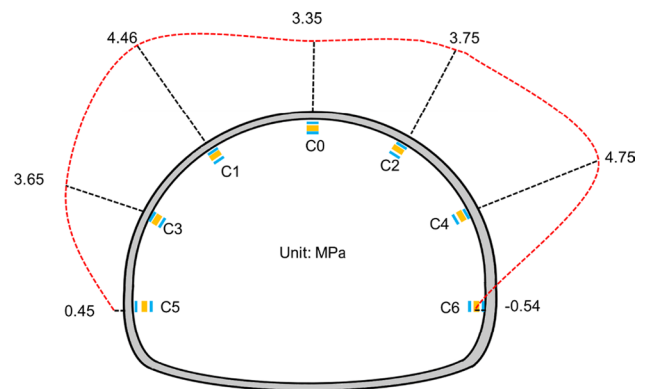

(a)

(b)

Fig. 12 The distribution curve of shotcrete stress over time at each monitoring section. **a** ZK53 + 830; **b** ZK53 + 900

Fig. 13 Maximum stress distribution of shotcrete in each monitoring section. **a** ZK53 + 830; **b** ZK53 + 900

of the second lining, greater pressure was required to fill the lining with concrete, while the high-pressure concrete transferred the pressure to the primary support. Compared with section ZK53 + 830, about 10 days after excavation, stress value at section ZK53 + 900 reached 75% of the maximum stress, because the concrete was the main force-bearing carrier in the early stage of excavation. After the completion of the second lining, the stress value at section ZK53 + 900 decreases obviously at first and then tends to be stable, because part of the stress borne by the shotcrete is transferred to the steel arch, and the reduction of the stress value of section ZK53 + 900is greater than that of section ZK53 + 830, which indicates that the second lining effect of the section at the fault fracture zone is better. Localized bulges and minor cracks on the primary support surface were observed at the construction site. Therefore, engineers should adjust the current support method in time for the tunnel construction, and the support mode of "flexible support first, rigid support second" can be adopted in the section with large geo-stress. In brief, the grid arch support with low stiffness is adopted in the first support, and the steel arch support is adopted in the second support to meet the

requirements of early rapid deformation of tunnel surrounding rock.

As shown in Fig. 13, as for the ZK53 + 830 section, the maximum stress of right arch shoulder was larger than the maximum stress of the left arch shoulder, but the pressure at left arch waist was higher than the pressure of right haunch. The section ZK53 + 900 was the opposite. As for the ZK53 + 830 section, the maximum compressive stress with the right shoulder was 3.84 MPa. A small tensile stress of 0.42 MPa occurred only at the left arch foot. The maximum compressive stress at the ZK53 + 900 section appeared at the right haunch, which was 4.75 MPa, while the arch right foot had small tensile stress. This proved that the spatial distribution of shotcrete stress was asymmetrical, mainly attributed to the tunnel arch as the main bearing component.

Development and distribution of steel arch support

Two sections were selected from the total monitoring sections to monitor initial support steel frame stress, numbered ZK53 + 920 and ZK53 + 950. There were seven measuring points in each monitoring section in Fig. 14. Figure 15 shows the steel arch's stress distribution curve with time. And Fig. 16 is the variation curve of the steel frame maximum stress at each monitoring section. The normal stress value of steel arch represents compressive stress, and vice versa is tensile stress.

As shown in Fig. 15, before the excavation, the stress on the steel frame's inner and outer sides at the ZK53 + 950 section increased fast, and the stress changes tended to level off after the second lining construction. Therefore, the second lining construction should be carried out as early as possible after the invert construction in the area affected by the fracture zones to reduce the concrete stress. The steel arch stress of the ZK53 + 920 section increased rapidly after the lower step excavation because the arch was in suspension due to the excavation of lower step. The inner and outer stress in
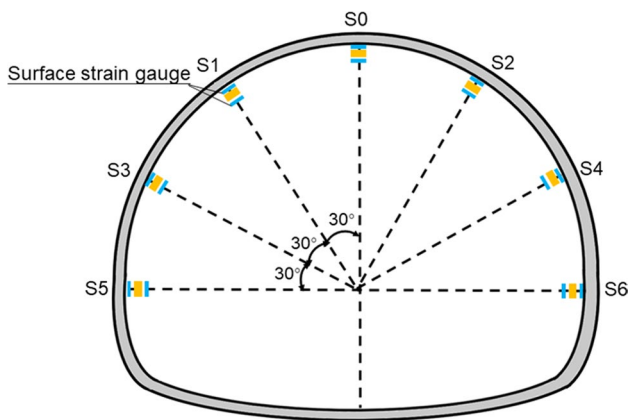
both monitored sections was asymmetrical about the tunnel axis, which may be related to the excavation environment, support timing and climatic conditions. The internal and external stress of the steel arch in section ZK53 + 920 is obviously greater than that in section ZK53 + 950. This is because the self-bearing capacity of the surrounding rock at the fault fracture zone is poor, and the steel arch needs to bear greater stress.

In Fig. 16, the stress on the steel arch's outer side at ZK53 + 920 section was greater than that at the ZK53 + 950 section, but the measured stress on the steel arch's inner side was the opposite. The stress difference of steel arch at Grade V surrounding rock was 0.77–3.66 times that at grade IV surrounding rock. At fault zones, the stress at the steel arch right shoulder was the highest, 260 MPa, which was higher than the compressive strength design value of the steel arch.

Development of stress between the primary support-secondary lining

Two sections were selected from the total monitoring sections for stress monitoring between primary support and secondary lining, numbered ZK53 + 920 and ZK53 + 950. There were five monitoring points in each monitoring section in Fig. 17. Figure 18 is the variation curve of contact stress over time at each monitoring section.

The stress monitoring of the primary and secondary lining of different monitoring sections starts on the second day of the secondary lining construction. In Fig. 18, the contact stress change of the two sections included three development stages: intense development stage, quick development stage and steady development stage. The stress at ZK 53 + 920 section was in the range of − 0.15 to 0.20 MPa. Moreover, the contact stress at ZK 53 + 950 section was in the range of − 0.05 to 0.25 MPa. In addition, at the ZK53 + 920 section, the stress of the left arch shoulder and right arch shoulder was unevenly distributed, with the stress values being 0.095 MPa and 0.15 MPa, respectively, in the stable development stage. This suggested that the joint and geo-stress tectonic action of surrounding rock were obvious. The stress of the two monitored sections was evenly distributed at the arch feet, so there was no stress concentration at the arch feet. Unlike the stress evolution law between rock mass-primary support, the contact stress at different measurement points in the two sections first increased sharply to a peak. Then it decreased rapidly in the intense development stage. In the second lining construction, the contact stress increases rapidly as the strength of the concrete increases rapidly during the setting process. Later, as the concrete hardened, its internal temperature decreased and its volume contracted, resulting in a gradual decrease in contact stress. And after the removal of the secondary lining formwork trolley, the contact stress gradually grows to stabilize. In the rapid


Fig. 14 The monitoring points of steel arch support

Fig. 15 Stress time history curve of the initial support steel frame. ▶
a ZK53＋950 (inner side of steel arch); **b** ZK53＋950 (outer side of steel arch); **c** ZK53＋920 (inner side of steel arch); **d** ZK53＋920 (outer side of steel arch)

development stage, the contact stress at ZK 53＋920 section and ZK 53＋950 section gradually increased. This showed that the pressure passed from the initial supporting to the secondary lining had a significant effect on the secondary lining following the hydrothermal chemical reaction of the concrete. Each monitoring section's measuring points' stress remained unchanged at about 40 days.

Conclusions

In this paper, based on the high geo-stress highway tunnel in fault fracture rock zone, excavation-induced tunnel deformation and stress responses of the rock mass and support structure were investigated by field monitoring tests. According to the research findings, the main conclusions are as under:

1. The tunnel is excavated by the up and down step method in the fault fracture zone, the tunnel arch subsidence and perimeter convergence were significantly asymmetric. The stable convergence value of upper step is 88.2 mm and the stable value of vault settlement is 53.1 mm, the former is about 1.56 times of the latter. Before the lower step excavation, the surrounding rock deformation is severe, and after the second lining is applied, the surrounding rock deformation is in the stable development stage. The results showed that secondary lining could effectively control tunnel subsidence in Class V rock mass section. The stiffness of tunnel support structure Class IV rock mass could be appropriately increased to control the tunnel deformation during the subsequent engineering construction.

2. The surrounding rock stress was mainly compression. The maximum surrounding rock stress in sections ZK53＋830 and ZK53＋880 was 0.234 MPa and 0.345 MPa, respectively. After the secondary lining was constructed, the changes in surrounding rock stress tended to stabilize, indicating that initial support and second lining shared rock mass loads. The stress was spatially presented as "greater at the vault and lower at the arch bottom". And the surrounding rock stress in the arch shoulder and arch waist was asymmetric about the tunnel axis, suggesting that the horizontal structural stress was significant.

3. The shotcrete stress in the section of the fault zone reached 75% of the maximum stress in about 10 days of excavation, and localized bulging and cracking of the primary support surface were observed at the con-
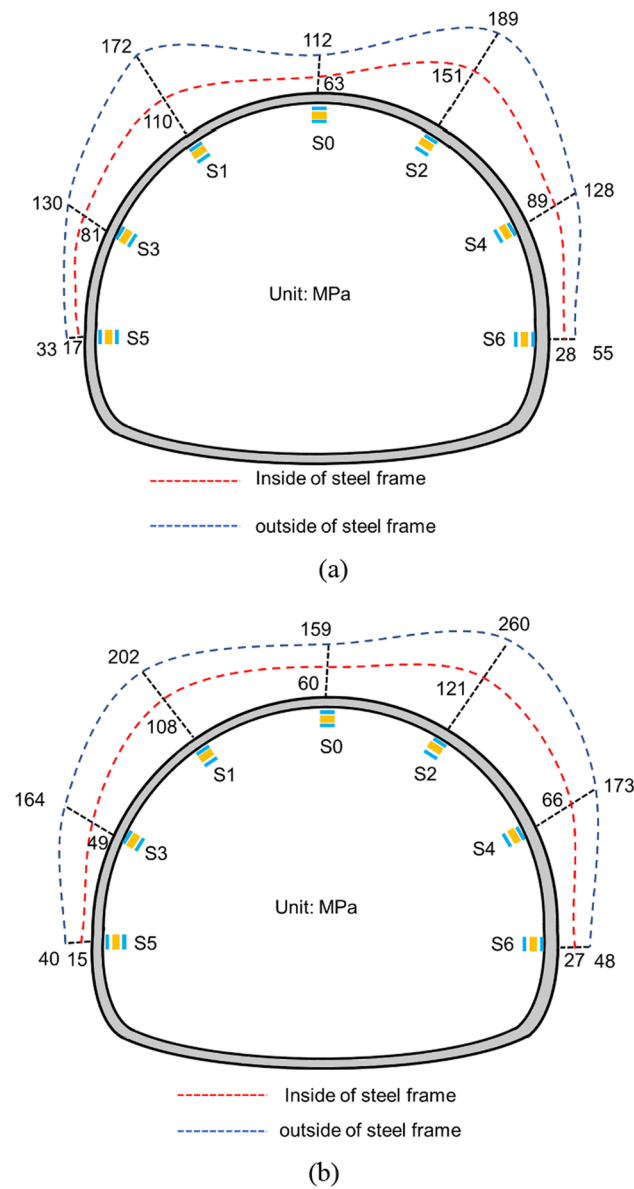
(a)

(b)
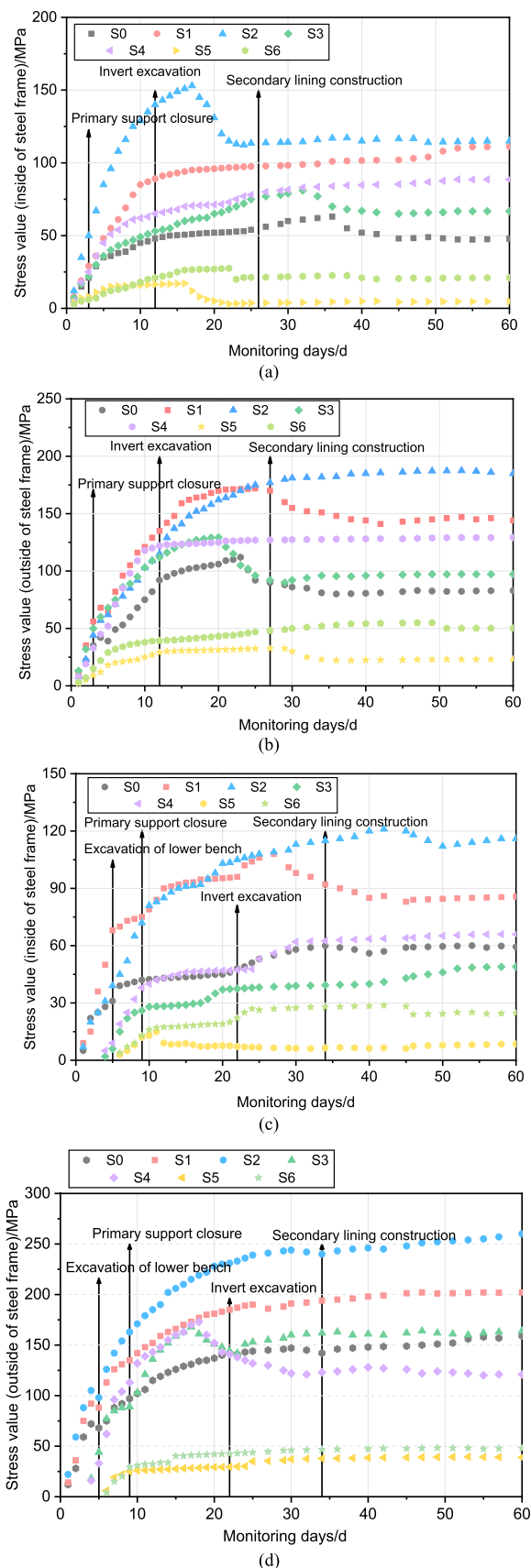
Fig. 16 Stress distribution of inside and outside of steel arch support on each monitoring section (unit: MPa). **a** ZK53+950; **b** ZK53+920

Fig. 17 The measurement points of stress

(a)

(b)

Fig. 18 The temporal distribution curve of initial support-secondary lining for each monitored section. **a** ZK53+920; **b** ZK53+950

struction site. The stress of steel arch frame reaches its peak about 1 month after excavation. Therefore, the surrounding rock stress is mainly borne by shotcrete in the early stage and steel arch in the later stage. In the area impacted by fault fracture zones, the construction of the second lining significantly reduced the rate of stress growth in the steel arch. Therefore, second lining construction should be carried out as soon as possible after the completion of the invert excavation in this area to reduce the arch stress.

4. A "flexible support first, rigid support second" type of support approach can be adopted at the high ground stress fault zone, i.e. the first support was a low stiffness
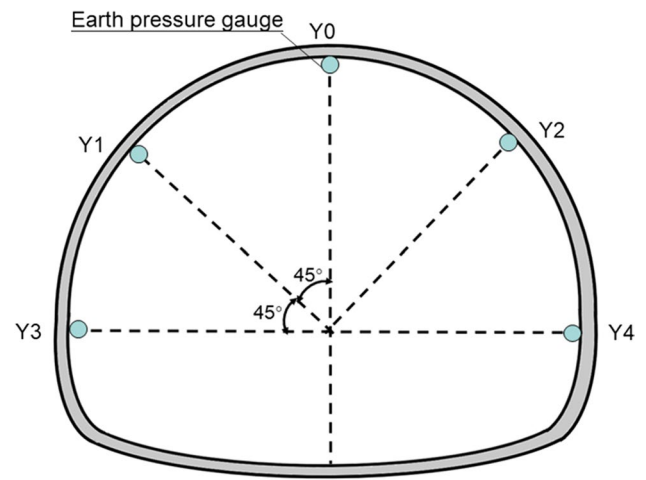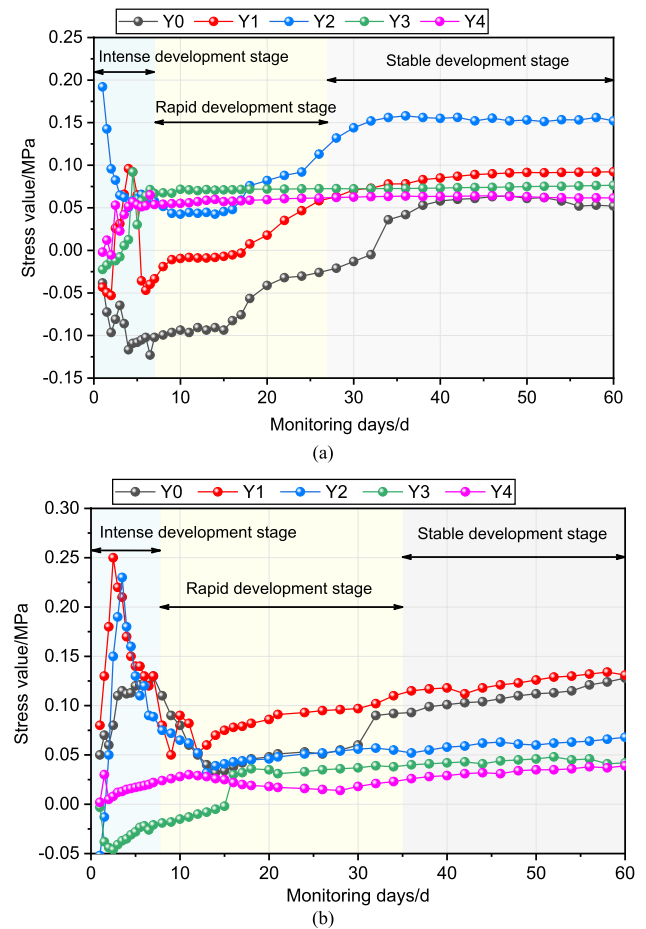
grid arch support and the secondary support was provided by a steel arch support to reduce the tunnel initial deformation better.

5. The fault zone section's initial supporting-second lining contact stress was asymmetrically distributed at the arch shoulders, with a maximum pressure of 0.15 MPa at the left shoulder and 0.95 MPa at the right arch shoulder. The joints and geo-stresses in the surrounding rock had obvious tectonic impacts.

Author contributions Rongming Zhou: writing - original draft and formal analysis; Xiaolin Weng: data curation and funding acquisition; Lin Li: formal analysis; Yanwei Guo：Investigation; Siyu Chen: resources; Xiaoming Huang: Methodology.

Data availability The authors confirm that the data supporting the findings of this study are available within the article.

Declarations

Conflict of interest All the authors declare that there are no known competing interests or personal relationships between them that would affect the publication of this article. And all have agreed with the author's order.

References

Aicha B, Mezhoud S (2021) Numerical modelling of the behavior of tunnel in soft surrounding rock: a case study of Djebel El-Ouahch tunnel, Algeria. Geotech Geol Eng 39(8):5505–5516. https://doi.org/10.1007/s10706-021-01841-9

Asghar R, Lohrasb F, Mohammad D (2017) Squeezing rock conditions at phyllite-slate zone in Golab water conveyance tunnel, Iran: a case study. J Cent South Univ 24(10):2475–2485. https://doi.org/10.1007/s11771-017-3659-6

Bayat M, Hamidi JK (2017) A case study on TBM tunnelling in fault zones and lessons learned from ground improvement. Tunn Undergr Space Technol 63:162–170. https://doi.org/10.1016/j.tust.2016.12.006

Bian K, Liu J, Liu Z, Liu S, Ai F, Zheng X, Ni S, Zhang W (2019) Mechanisms of large deformation in soft rock tunnels: a case study of Huangjiazhai Tunnel. Bull Eng Geol Environ 78(1):431–444. https://doi.org/10.1007/s10064-017-1155-8

Chen ZQ, He C, Xu GW, Ma GY, Wu D (2019a) A Case Study on the Asymmetric Deformation Characteristics and Mechanical Behavior of Deep-Buried Tunnel in Phyllite. Rock Mech Rock Eng 52:4527–4545. https://doi.org/10.1007/s00603-019-01836-2

Chen ZQ, He C, Xu GW, Ma GY, Yang WB (2019b) Supporting mechanism and mechanical behavior of a double primary support method for tunnels in broken phyllite under high geo-stress: a case study. Bull Eng Geol Environ 78:5253–5267. https://doi.org/10.1007/s10064-019-01479-1

Chen ZY, Wang ZX, Su GS, Gao S, Hu XC (2022) Construction technology of micro bench cut method for weak rock tunnel with high in-situ stress. Geotech Geol Eng 40:1407–1415. https://doi.org/10.1007/s10706-021-01971-0

Das AJ, Mandal PK, Sahu SP, Kushwaha A, Bhattacharjee R, Tewari S (2018) Evaluation of the effect of fault on the stability of underground workings of coal mine through DEM and statistical analysis. J Geol Soc India 92(6):732–742. https://doi.org/10.1007/s12594-018-1096-2

Deng HS, Fu HL, Shi Y, Zhao YY, Hou WZ (2022) Countermeasures against large deformation of deep-buried soft rock tunnels in areas with high geo-stress: a case study. Tunn Undergr Space Technol 119:104238. https://doi.org/10.1016/j.tust.2021.104238

Dwivedi RD, Singh M, Viladkar MN, Goel RK (2013) Prediction of tunnel deformation in squeezing grounds. Eng Geol 161:55–64. https://doi.org/10.1016/j.enggeo.2013.04.005

Gao Y, Jiang YJ, Li B (2014) Estimation of effect of voids on frequency response of mountain tunnel lining based on microtremor method. Tunn Undergr Space Technol 42:184–194. https://doi.org/10.1016/j.tust.2014.03.004

Gattinoni P, Consonni M, Francani V, Leonelli G, Lorenzo C (2019) Tunnelling in landslide areas connected to deep seated gravitational deformations: an example in Central Alps (northern Italy). Tunn Undergr Space Technol 93:103100. https://doi.org/10.1016/j.tust.2019.103100

Gisbert J, Vallejos A, Gonzalez A, Pulido-Bosch A (2009) Environmental and hydrogeological problems in karstic terrains crossed by tunnels: a case study. Environ Geol 58:347–357. https://doi.org/10.1007/s00254-008-1609-1

Jeon S, Kim J, Seo Y, Hong C (2004) Effect of a fault and weak plane on the stability of a tunnel in rock—a scaled model test and numerical analysis. Int J Rock Mech Min Sci 41:658–663. https://doi.org/10.1016/j.ijrmms.2003.12.021

Lai HP, Song WL, Liu YU, Chen R (2017) Influence of flooded loessial overburden on the tunnel lining: case study. J Perform Constr Facil. https://doi.org/10.1061/(ASCE)CF.1943-5509.0001100

Li D, Fu LZ, Sheng LY (2011) Research on the mechanical characteristics of primary supports in Guanjiao tunnel fault fracture zone and its influence zone by field tests. Appl Mech Mater 105:1203–1210. https://doi.org/10.4028/www.scientific.net/AMM.105-101.1203

Li HY, Li XG, Yang Y, Ma MZ (2022) Structural stress characteristics and joint deformation of shield tunnels crossing active faults. Appl Sci Basel 12:3229. https://doi.org/10.3390/app12073229

Lia JX, Wang XL, Qiu JL, Chen JX, Hu ZN, Wang H (2018) Extreme deformation characteristics and countermeasures for a tunnel in difficult grounds in southern Shaanxi, China. Environ Earth Sci 77:19. https://doi.org/10.1007/s12665-018-7888-2

Lin DM, Yuan RM, Shang YJ, Bao WX, Wang KY, Zhang ZJ, Li K, He WT (2017) Deformation and failure of a tunnel in the restraining bend of a strike–slip fault zone: an example from Heng shan Mountain, Shanxi Province, China. Bull Eng Geol Environ 76:263–274. https://doi.org/10.1007/s10064-016-0850-1

Liu ZW, Wang MS, Fang JB (2010) In-situ study of reinforcement systems for tunnels under high geo-stress and large deformation. Chin Civ Eng J 43(5):111–116 (**In Chinses**)

Maleki MR, Dehnavi RN (2018) Influence of discontinuities on the squeezing intensity in high in situ stresses (a tunnelling case study; actual evidences and TBM release techniques). Rock Mech Rock Eng 51(9):2911–2933. https://doi.org/10.1007/s00603-018-1476-3

Malkowski P, Ostrowski L, Bachanek P (2017) Modelling the small throw fault effect on the stability of a mining roadway and its verification by in situ investigation. Energies 10:12. https://doi.org/10.3390/en10122082

Manasa H, Maji VB (2023) A numerical study on the effect of different tunnel shapes in squeezing rocks. Indian Geotech J. https://doi.org/10.1007/s40098-023-00782-9

Meng LB, Li TB, Jiang Y, Wang R, Li Y (2013) Characteristics and mechanisms of large deformation in the Zhegu mountain tunnel on the Sichuan-Tibet highway. Tunn Undergr Space Technol 37:157–164. https://doi.org/10.1016/j.tust.2013.03.009

National standards of the People's Republic of China (1995) GB50218-94 Engineering rock mass classification standard. China Planning Press, Beijing (**In Chinese**)

Qian DY, Zhang N, Zhang MW, Shimada H, Cao P, Chen YL, Wen K, Yang S, Zhang NC (2017) Application and evaluation of ground surface pre-grouting reinforcement for 800-m-deep underground opening through large fault zones. Arab J Geosci 10:13. https://doi.org/10.1007/s12517-017-3052-7

Qin YW, Lai JX, Gao GQ, Yang T, Zan WB, Feng ZH, Liu T (2022) Failure analysis and countermeasures of a tunnel constructed in loose granular stratum by shallow tunnelling method. Eng Fail Anal 141:106667. https://doi.org/10.1016/j.engfailanal.2022.106667

Qiu WG, Ai XF, Zheng YC (2022) First application of mechanized method using earth pressure balance TBM with large horseshoe-shaped cross section to loess mountain tunnel: a case study of Baicheng tunnel. Tunn Undergr Space Technol 126:104547. https://doi.org/10.1016/j.tust.2022.104547

Roy CK, Uddin MG, Roy B, Dean TR (2017) Evaluating aspect mining techniques: a case study. 15th IEEE international conference on program comprehension, Banff, Canada, pp 167. https://doi.org/10.1109/ICPC.2007.21

Su GS, Fu XY (2009) Study on support type for weak zone of diversion tunnel under high geo-stress and high seepage pressure condition. International Forum on Porous Flow and Applications, Wuhan

Tang BL, Ren YQ (2021) Study on seismic response and damping measures of surrounding rock and secondary lining of deep tunnel. Shock Vib. https://doi.org/10.1155/2021/7824527

Wang MY, Zhang N, Li J, Ma LJ, Fan PX (2015) Computational method of large deformation and its application in deep mining tunnel. Tunn Undergr Space Technol 50:47–53. https://doi.org/10.1016/j.tust.2015.06.006

Wang FT, Zhang C, Wei SF, Zhang XG, Guo SH (2016) Whole section anchor–grouting reinforcement technology and its application in underground roadways with loose and fractured surrounding rock. Tunnel Undergr Space Technol 51:133–143. https://doi.org/10.1016/j.tust.2015.10.029

Wang YC, Jing HW, Su HJ, Xie JY (2017a) Effect of a fault fracture zone on the stability of tunnel-surrounding rock. Int J Geomech. https://doi.org/10.1061/(ASCE)GM.1943-5622.0000837

Wang YQ, Xin YX, Xie YL, Li J, Wang Z (2017b) Investigation of mechanical performance of prestressed steel arch in tunnel. Front Struct Civ Eng 11(3):360–367. https://doi.org/10.1007/s11709-017-0429-3

Wang YQ, Chang HT, Wang JY, Shi XL, Qiu JL (2019) Countermeasures to treat collapse during the construction of road tunnel in fault zone: a case study from the Yezhuping tunnel in south Qinling, China. Environ Earth Sci 78:15. https://doi.org/10.1007/s12665-019-8481-z

Wu H, Fan FF, Yang XH, Wang ZC, Lai JX, Xie YL (2022) Large deformation characteristics and treatment effect for deep bias tunnel in broken phyllite: a case study. Eng Fail Anal. https://doi.org/10.1016/j.engfailanal.2022.106045

Xu SS, Ma EL, Lai JX, Yang YT, Liu HT, Yang CP, Hu Q (2022) Diseases failures characteristics and countermeasures of expressway tunnel of water-rich strata: a case study. Eng Fail Anal. https://doi.org/10.1016/j.engfailanal.2022.106056

Yang SQ, Chen M, Jing HW, Chen KF, Meng B (2017) A case study on large deformation failure mechanism of deep soft rock roadway in Xin' an coal mine, China. Eng Geol 217:89–101. https://doi.org/10.1016/j.enggeo.2016.12.012

Zhang CQ, Cui GJ, Zhang Y, Zhou H, Liu N, Huang SL (2020) Squeezing deformation control during bench excavation for the Jinping deep soft-rock tunnel. Eng Fail Anal 116:104761. https://doi.org/10.1016/j.engfailanal.2020.104761

Zhang YX, Yuan MQ, Lu WH, Zhang J (2022) Cause investigation of ground sliding during tunneling in sloping and stratified stratum. Nat Hazards 111:1421–1430. https://doi.org/10.1007/s11069-021-05102-z

Zhong ZL, Wang Z, Zhao M, Du XL (2020) Structural damage assessment of mountain tunnels in fault fracture zone subjected to multiple strike-slip fault movement. Tunn Undergr Space Technol 104:103527. https://doi.org/10.1016/j.tust.2020.103527

Zhou ZH, Chen ZQ, He C, Kou H (2021a) Investigation on the evolution characteristics and transfer mechanism of surrounding rock pressure for a hard-rock tunnel under high geo-stress: case study on the Erlang Mountain Tunnel, China. Bull Eng Geol Environ 80:8339–8361. https://doi.org/10.1007/s10064-021-02439-4

Zhou ZL, Zhao JP, Tan ZS, Zhou XP (2021b) Mechanical responses in the construction process of super-large cross-section tunnel: a case study of Gongbei tunnel. Tunnel Undergr Space Technol. https://doi.org/10.1016/j.tust.2021.104044